

High-order harmonic generation from gapped graphene: perturbative response and transition to non-perturbative regime

Darko Dimitrovski,¹ Lars Bojer Madsen,² and Thomas Garm Pedersen¹

¹*Department of Physics and Nanotechnology, Aalborg University, Skjernvej 4A 9220 Aalborg East, Denmark**

²*Department of Physics and Astronomy, Aarhus University, Ny Munkegade 120, 8000 Aarhus C, Denmark*

(Dated: October 8, 2018)

We consider the interaction of gapped graphene in the two-band approximation using an explicit time-dependent approach. In addition to the full high-order harmonic generation (HHG) spectrum, we also obtain the perturbative harmonic response using the time-dependent method at photon energies covering all the significant features in the responses. The transition from the perturbative to the fully non-perturbative regime of HHG at these photon energies is studied in detail.

PACS numbers: 42.65.Ky, 72.20.Ht, 42.50.Hz

I. INTRODUCTION

The interaction of strong lasers with solids has been studied since the early days of strong-field physics [1]. Recently, due to the development of short, strong laser pulses with controlled waveforms [2], it has become relevant to consider the response of such materials to strong laser pulses with respect to the transferred charge [3, 4], and the generated harmonic radiation [5, 6]. As the pulses used in these studies are strong and short, they come almost exclusively from (near) infrared sources.

A material of special interest is graphene. The properties of graphene, such as its stability and the huge mobility of carriers, promise a plethora of nanoscale electronic applications [7]. Concerning harmonic radiation by strong laser fields, in the past HHG in graphene was considered by directly applying the strong-field approximation [1, 8] for graphene described on the level of molecular orbitals [9, 10]. HHG in graphene was also considered performing time domain calculations that took into account the inter- and intraband dynamics for THz pulses and in the Dirac approximation [11, 12], and calculations investigating multiphoton resonant excitation [13–15]. Another very active area of research is the investigation of the third harmonic generation in graphene, for recent results, see e.g., [16, 17]. Graphene is, however, a semimetal with a zero band gap, and that limits the possible applications in electronic and optoelectronic devices. Fortunately a class of materials, termed gapped graphene, based on or similar to graphene was developed using various techniques [18–22]. Gapped graphene can be described within the two-band tight-binding approximation [23]. This enabled extensive theoretical studies of optical response of this system including the linear [23, 24] and beyond linear response [25], second harmonic generation [26], third harmonic response [27, 28] and magneto optics [29].

Of particular interest is the ability of the theory to identify the breakdown of perturbation theory and to

deal directly with the explicit time-dependence of the pulse. Here we therefore consider high-order harmonic generation spectra for gapped graphene from the perturbative optical response and into the non-perturbative regime. In particular, we consider the first, second and third harmonic responses using a time-dependent approach and investigate the breakdown of perturbation theory.

The paper is organized as follows. In the next section we present the basic structure and the equations for the two-band model of gapped graphene. In Sec. III we present the basics of the interaction of a two-band system with light, including the way to calculate high-order harmonic generation (HHG) spectra. In Sec. IV we compare the harmonic response to the perturbative harmonic response for gapped graphene. The transition from the perturbative harmonic response to the non-perturbative HHG spectra is considered in Sec. V, where we also consider the gap dependence. We conclude in the last section. The expressions for the dipole couplings and momentum matrix elements within and between the bands of gapped graphene are given in the Appendices.

II. STRUCTURE AND BASIC EQUATIONS

The structure of graphene, and also of gapped graphene, which is identical in position space, is given in Fig. 1. The elementary lattice vectors, shown in Fig. 1, are [30]

$$\mathbf{a}_1 = \frac{a}{2} \begin{pmatrix} \sqrt{3} \\ 1 \end{pmatrix}, \quad \mathbf{a}_2 = \frac{a}{2} \begin{pmatrix} \sqrt{3} \\ -1 \end{pmatrix}, \quad (1)$$

where $a = 2.46 \text{ \AA}$ is the lattice constant.

To obtain the electronic band structure, we use the p_z atomic orbitals at the atomic sites A and B [Fig. 1], $|p_z(\mathbf{r} - \mathbf{R}_A)\rangle$ and $|p_z(\mathbf{r} - \mathbf{R}_B)\rangle$. Then we form Bloch wave functions $|\alpha\rangle = \frac{1}{\sqrt{N}} \sum_{\mathbf{R}} e^{i\mathbf{k}\cdot(\mathbf{R}_A + \mathbf{R})} |p_z(\mathbf{r} - (\mathbf{R}_A + \mathbf{R}))\rangle$ and $|\beta\rangle = \frac{1}{\sqrt{N}} \sum_{\mathbf{R}} e^{i\mathbf{k}\cdot(\mathbf{R}_B + \mathbf{R})} |p_z(\mathbf{r} - (\mathbf{R}_B + \mathbf{R}))\rangle$, where

* dd@nano.aau.dk

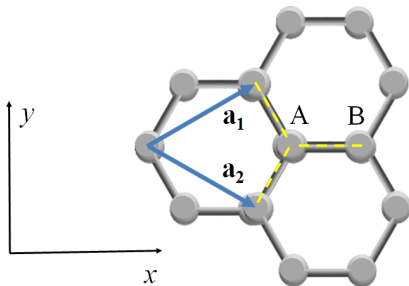


FIG. 1. The structure of graphene and gapped graphene in position space. The elementary lattice vectors, \mathbf{a}_1 and \mathbf{a}_2 , as well as the atomic sites A and B (the two inequivalent sublattices) are shown. The yellow dashed lines denote the connections of A with its nearest neighbors. The x and y axes are also indicated.

$N \rightarrow \infty$ is the number of unit cells, and the sum runs over the Bravais lattice vectors \mathbf{R} , and \mathbf{k} is the wave vector.

A band gap in graphene can be induced in several ways: graphene grown on SiC substrate [18], biasing a graphene bilayer [19], sculpturing a graphene into nanoribbons [20], or introducing a periodic array of circular holes [21, 22]. In addition, systems like hexagonal BN, where 2 carbon atoms in the unit cell are replaced by a BN dimer, can be described using the same model as gapped graphene with respect to the interaction with light [31]. Here we focus on the class of gapped graphene where the inversion symmetry is broken, such as graphene grown on the SiC surface and the BN. For this type of gapped graphene, similarly to graphene [30], using $|\alpha\rangle$ and $|\beta\rangle$ and assuming nearest-neighbor coupling, the tight-binding Hamiltonian is obtained as [23]

$$\hat{H}_0 = \begin{bmatrix} \frac{\Delta}{2} & -\gamma f(\mathbf{k}) \\ -\gamma f^*(\mathbf{k}) & -\frac{\Delta}{2} \end{bmatrix}, \quad (2)$$

where Δ is the energy gap, $\gamma = -\langle p_z(\mathbf{r} - \mathbf{R}_A) | \hat{H} | p_z(\mathbf{r} - \mathbf{R}_B) \rangle \approx 3 \text{ eV}$ is the hopping integral and

$$f(\mathbf{k}) = \exp\left(i\frac{ak_x}{\sqrt{3}}\right) + 2\exp\left(-i\frac{ak_x}{2\sqrt{3}}\right) \cos\left(\frac{ak_y}{2}\right) \quad (3)$$

comes from the geometry of the location of the nearest neighbors, see Fig. 1, i.e., from the addition of factors of a type $\exp(i\mathbf{k} \cdot (\mathbf{R}_A - \mathbf{R}_B))$. Diagonalizing the Hamiltonian of Eq. (2) we recover the valence band

$$E_v(\mathbf{k}) = -\sqrt{\left(\frac{\Delta}{2}\right)^2 + \gamma^2 |f(\mathbf{k})|^2} \quad \text{and the conduction band} \\ E_c(\mathbf{k}) = \sqrt{\left(\frac{\Delta}{2}\right)^2 + \gamma^2 |f(\mathbf{k})|^2}.$$

III. INTERACTION WITH LIGHT IN THE DIPOLE APPROXIMATION FOR A TWO-BAND SYSTEM

For a two-band system, such as the one obtained using the tight-binding approximation, the wavefunction can be written as

$$\Psi(\mathbf{r}, t) = \sum_{m=c,v} \int_{\text{BZ}} a_m(\mathbf{k}, t) \psi_{m,\mathbf{k}}(\mathbf{r}) d^3\mathbf{k}, \quad (4)$$

where BZ denotes that the integration is performed over the Brillouin zone, c and v denote conduction and valence bands, respectively, and

$$\psi_{m,\mathbf{k}}(\mathbf{r}) = u_{m\mathbf{k}}(\mathbf{r}) \exp(i\mathbf{k} \cdot \mathbf{r}) \quad (5)$$

are the Bloch wave functions - eigenfunctions of the field-free Hamiltonian \hat{H}_0 , i.e., $\hat{H}_0 \psi_{m,\mathbf{k}} = E_m(\mathbf{k}) \psi_{m,\mathbf{k}}(\mathbf{r})$. The field-free Hamiltonian \hat{H}_0 , which can describe any two-band system, refers here to the Hamiltonian written in matrix form in Eq. (2).

When interacting with light, in the length gauge, $\hat{H}(t) = \hat{H}_0 + e\mathbf{F}(t) \cdot \mathbf{r}$, where $\mathbf{F}(t)$ is the electric field of the laser and e is the norm of the electron charge. The a_m 's from Eq. (4) satisfy the following equations of motion [32]

$$\dot{a}_m = \left(-\frac{i}{\hbar} E_m(\mathbf{k}) + \frac{e}{\hbar} \mathbf{F}(t) \cdot \nabla_{\mathbf{k}} \right) a_m - i \frac{e}{\hbar} \mathbf{F}(t) \cdot \sum_n \boldsymbol{\xi}_{mn}(\mathbf{k}) a_n \quad (6)$$

where

$$\boldsymbol{\xi}_{mn}(\mathbf{k}) = i \int u_{m\mathbf{k}}^*(\mathbf{r}) \nabla_{\mathbf{k}} u_{n\mathbf{k}}(\mathbf{r}) d^3\mathbf{r}, \quad (7)$$

$n, m \in (c, v)$, and where the dependence of a_m and a_n on k and t is omitted to ease notation. The explicit expressions for the $\boldsymbol{\xi}$'s of Eq. (7) are given in Appendix A.

The amplitude equations (6) do not readily allow inclusion of decoherence and temperature effects. For this purpose, we reformulate the equations of motion using the density matrix to arrive at

$$i\hbar \frac{d\rho}{dt} = [\hat{H}_0 + e\mathbf{F} \cdot \mathbf{r}, \rho], \quad (8)$$

where

$$[\hat{H}_0, \rho]_{nm} = (E_n - E_m) \rho_{nm} \quad (9)$$

and, following [32],

$$[\mathbf{r}^{(i)}, \rho]_{nm} = i \nabla_{\mathbf{k}} \rho_{nm} + \rho_{nm} (\boldsymbol{\xi}_{nn} - \boldsymbol{\xi}_{mm}). \quad (10)$$

Inserting Eqs. (9) and (10) in Eq. (8) and adding a term containing the decoherence times, τ_1 for ρ_{cv} and τ_2 for n , to introduce a decay, we obtain the following coupled equations of motion

$$\frac{d\rho_{cv}(\mathbf{k}, t)}{dt} = -i\omega_{cv}(\mathbf{k})\rho_{cv}(\mathbf{k}, t) - i\frac{e}{\hbar}\mathbf{F}(t) \cdot \boldsymbol{\xi}_{cv}(\mathbf{k})n(\mathbf{k}, t) + \frac{e}{\hbar}\mathbf{F}(t) \cdot \nabla_{\mathbf{k}}\rho_{cv}(\mathbf{k}, t) - i\frac{e}{\hbar}\mathbf{F}(t) \cdot (\boldsymbol{\xi}_{cc}(\mathbf{k}) - \boldsymbol{\xi}_{vv}(\mathbf{k}))\rho_{cv}(\mathbf{k}, t) - \frac{\rho_{cv}(\mathbf{k}, t)}{\tau_1} \quad (11)$$

and

$$\frac{dn(\mathbf{k}, t)}{dt} = 2i\frac{e}{\hbar}\mathbf{F}(t) \cdot (\boldsymbol{\xi}_{cv}(\mathbf{k})\rho_{cv}^*(\mathbf{k}, t) - \boldsymbol{\xi}_{cv}^*(\mathbf{k})\rho_{cv}(\mathbf{k}, t)) + \frac{e}{\hbar}\mathbf{F}(t) \cdot \nabla_{\mathbf{k}}n(\mathbf{k}, t) - \frac{n(\mathbf{k}, t) - (f_v(\mathbf{k}) - f_c(\mathbf{k}))}{\tau_2}, \quad (12)$$

where $n = \rho_{vv} - \rho_{cc}$, $\omega_{cv} = \frac{E_c - E_v}{\hbar}$, and

$$f_{c/v}(\mathbf{k}, T) = \left(1 + \exp\left(\frac{E_{c/v}(\mathbf{k})}{k_B T}\right)\right)^{-1} \quad (13)$$

is the Fermi-Dirac distribution for the conduction and valence band, respectively. In the above equation, k_B is Boltzmann's constant, and T is the temperature.

The equations of motion, (11) and (12), are solved with the initial conditions $\rho_{cv}(\mathbf{k}, -\infty) = 0$ and $n(\mathbf{k}, -\infty) = f_v(\mathbf{k}, T) - f_c(\mathbf{k}, T)$. The numerical approach for solving the above equations is based on Ref. [11]: we use a \mathbf{k} grid and approximate the gradients with balanced difference. The time propagation is performed using an adaptive Runge-Kutta algorithm. As in Ref. [11], we use $T = 10$ K throughout.

A. Calculating the current and the HHG spectrum

The current density, to be referred to simply as the current throughout, is given by $\mathbf{J}(t) = -2\frac{e}{m_e}\text{Tr}\{\hat{\mathbf{p}}\rho\}$, where the factor of 2 stands for the spin multiplicity. The current is explicitly calculated as

$$\mathbf{J}(t) = -\frac{e}{2\pi^2 m_e} \left[\int d\mathbf{k} (\mathbf{p}_{vc}(\mathbf{k})\rho_{cv}(\mathbf{k}, t) + \mathbf{p}_{cv}(\mathbf{k})\rho_{vc}(\mathbf{k}, t)) + \int d\mathbf{k} \frac{1}{2} (\mathbf{p}_{vv}(\mathbf{k}) - \mathbf{p}_{cc}(\mathbf{k}))n(\mathbf{k}, t) \right] \quad (14)$$

The first integral in the above equation represents the interband current, while the second integral the intraband current. The momentum matrix elements appearing in the expression for the current are obtained as follows. The diagonal momentum matrix elements are obtained as

$$\mathbf{p}_{nn} = \frac{m_e}{\hbar} \frac{\partial E_n}{\partial \mathbf{k}},$$

while the off-diagonal matrix elements can be obtained as either $\mathbf{p}_{nm} = \frac{m_e}{\hbar} \left\langle n\mathbf{k} \left| \frac{\partial \hat{H}}{\partial \mathbf{k}} \right| m\mathbf{k} \right\rangle$

[33, 34] or $\mathbf{p}_{nm} = im_e\omega_{nm}\boldsymbol{\xi}_{nm}$ [32]. The explicit expressions for the momentum matrix elements are given in Appendix B.

The harmonic spectrum is obtained as $|\mathbf{j}(\Omega)|^2$, where $\mathbf{j}(\Omega) = \mathcal{F}\{\mathbf{J}(t)\}$ is the Fourier transform of the current. In practice we consider the component of the current along one direction, in our case the x -component of the

current [Fig. 1], and present the discrete Fourier transform of the current

$$j(\Omega) = \sum_{k=0}^{N_p-1} J_k \exp(i\Omega t_k), \quad (15)$$

where N_p is the number of points for current samples (J_k) and time samples (t_k). We use a laser pulse, defined by the electric field vector

$$\mathbf{F}(t) = \mathbf{F}_0 \exp\left[-\left(\frac{t - MT_p/2}{MT_p/6}\right)^2\right] \sin\left(\frac{2\pi}{T_p}t\right) \quad (16)$$

for $t \in [0, MT_p]$,

where $F_0 = |\mathbf{F}_0|$ is the peak electric field strength, $T_p = 2\pi/\omega$ is the period of the field, with ω the driving frequency, and M is the number of the field cycles. The exponential factor in Eq. (16) describes the envelope and the sinusoidal factor the carrier of the pulse. We express the peak field strength in atomic units (a.u.) - 1 a.u. of field strength is 5.142×10^{11} V/m. The Fourier transform of the field scaled by its duration (MT_p), in the limit of infinitely large pulse ($M \rightarrow \infty$) and for each ω is proportional to a δ function in Fourier space. This scaling is exploited for the current - the expression (15) does not depend on the pulse duration explicitly therefore in the limit of infinitely long pulses (15) is proportional to the Fourier transform of the current caused by an infinite periodic pulse. Finally, in this way, the discrete Fourier transform of the current (15) has the same dimension as the current.

IV. PERTURBATIVE HARMONIC RESPONSE

We consider the harmonic responses of gapped graphene, traditionally investigated using frequency-domain methods [35], using explicitly time-dependent methods. We do this to test our numerical solution and to investigate the breakdown of perturbation theory.

For illustrative calculations, capturing generic effects in gapped graphene, we consider a gap of 1 eV. To ensure that well-defined harmonic peaks appear we perform calculations using pulses described by Eq. (16) with $M = 48$ cycles. Next, to stabilize the numerical calculations and ensure rapid convergence we choose a relatively small value of the decoherence time $\tau_1 = \tau_2 = 5$ fs. We

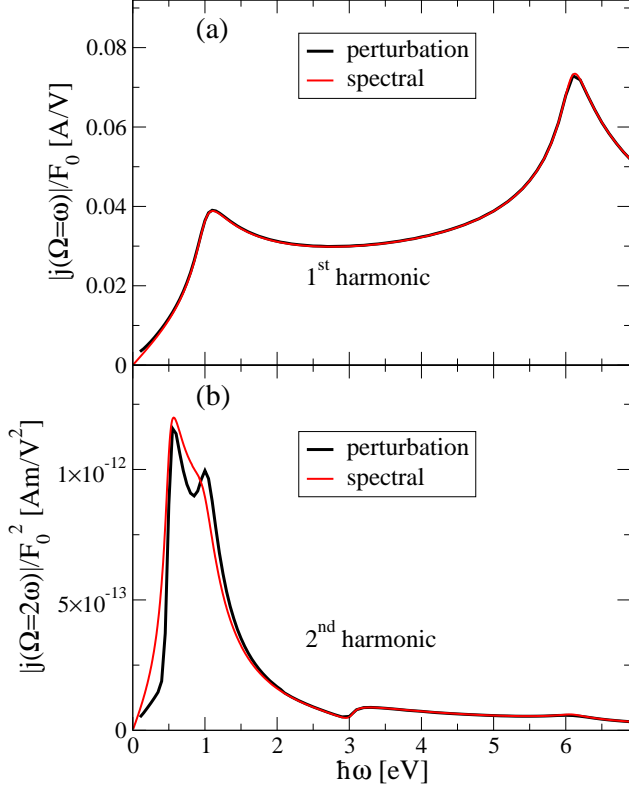


FIG. 2. The absolute value of the (a) first harmonic (linear response) and (b) second harmonic, for 1 eV gapped graphene and $\tau_1 = \tau_2 = 5$ fs obtained using the time-dependent calculation for $M = 48$ cycles (black curves) and the frequency-dependent method for infinitely periodic pulses.

orient the field along the x -axis [see Fig. 1] so that both odd and even harmonics appear. To extract the first and the second harmonic response from the numerical calculations we first obtain the full harmonic spectrum for a fixed driving frequency ω and then select only the value at the first and second harmonic, and repeat the procedure, changing ω in small steps to ensure that all the features in the harmonic responses are captured.

The perturbative result in the time domain is obtained by expanding ρ_{cv} in orders of field strength as ($\rho_{cv}^{(0)} = 0$ trivially)

$$\rho_{cv}(\mathbf{k}, t) = \sum_{j=1}^{\infty} F_0^j \rho_{cv}^{(j)}(\mathbf{k}, t), \quad (17)$$

Inserting the condition of (19) into Eq. (11) we obtain

the following coupled system of equations

$$\begin{aligned} \frac{d\rho_{cv}^{(1)}}{dt} &= -i\omega_{cv}\rho_{cv}^{(1)} - i\frac{e}{\hbar}\Delta f_{vc}(\mathbf{k})\mathbf{f}(t) \cdot \boldsymbol{\xi}_{cv} - \frac{\rho_{cv}^{(1)}}{\tau_1} \\ \frac{d\rho_{cv}^{(j)}}{dt} &= -i\omega_{cv}\rho_{cv}^{(j)} - \frac{\rho_{cv}^{(j)}}{\tau_1} - i\frac{e}{\hbar}\mathbf{f}(t) \cdot (\boldsymbol{\xi}_{cc} - \boldsymbol{\xi}_{vv})\rho_{cv}^{(j-1)} \\ &\quad + \frac{e}{\hbar}(\mathbf{f}(t) \cdot \nabla_{\mathbf{k}})\rho_{cv}^{(j-1)} \quad \text{for } j \geq 2, \end{aligned} \quad (18)$$

where $\mathbf{f}(t) = \mathbf{F}(t)/F_0$ is the normalized field. The first two coupled equations (for $j = 1$ and $j = 2$), that are independent of the peak field strength, are solved putting $\tau_1 = \tau_2 = 5$ fs to obtain the perturbative responses for the first and the second harmonic in Figs. 2-4.

We briefly review the features in the perturbative first and second harmonic response. The absolute value of the linear response (first harmonic) [Fig. 2 (a)] has peaks for photon energies corresponding to the gap $\Delta = 1$ eV and to the van Hove singularity [36](M point - the point where $\nabla_{\mathbf{k}}E_{c/v}(\mathbf{k}) = 0$) at a photon energy of $2\sqrt{(\Delta/2)^2 + \gamma^2|f(\mathbf{k})|^2} = 6.2$ eV. The second harmonic response [Fig. 2 (b)], in addition to the peaks at the gap and the van Hove singularity, should exhibit peaks at half of these photon energies corresponding to two-photon transitions. It is evident from Fig. 2 that the peaks corresponding to the van Hove singularity and to the half of this frequency are very weak.

Next, we compare our perturbative solution obtained in the time domain for $M = 48$ cycles [black curves in Fig. 2], with the corresponding solution for an infinite periodic field, obtained using frequency-domain methods, as done in Ref. [26], using $\tau_1 = \tau_2 = 5$ fs (red curves in Fig. 2). To compare directly, the latter result is scaled (but not fitted) using appropriate factors to the time-domain solution. This factor involves $N_p/2$ coming from the Fourier transform [Eq. (15)] and a factor coming from the consideration of the limit of the type $\lim_{\epsilon \rightarrow 0} \exp(-\omega^2/\epsilon^2)/(\epsilon\sqrt{\pi}) = \delta(\omega)$ for the Fourier transform of the envelope of the pulse [Eq. (16)] (for the linear response) and the square of the Fourier transform (for the second harmonic). As evident from Fig. 2, the agreement between the two types of solution is very good. There are differences between the two methods at the peaks for the second harmonic, whereas for photon energies away from the peaks the agreement between the two methods is excellent.

The value of the time-domain perturbative solution is that incorporates the finite pulse duration, so that a full numerical solution for a finite number of cycles can be compared to it to gauge the departure from the perturbative regime. In particular, we compare the numerical solution with the solution in the perturbative limit, that we also obtain numerically, for the first, second and the third harmonic, and at photon energies covering all significant features of the responses.

In the first set of results that we present, we perform numerical calculation neglecting the time dependency of n , i.e., we use Eqs. (11) and (12) keeping the time-

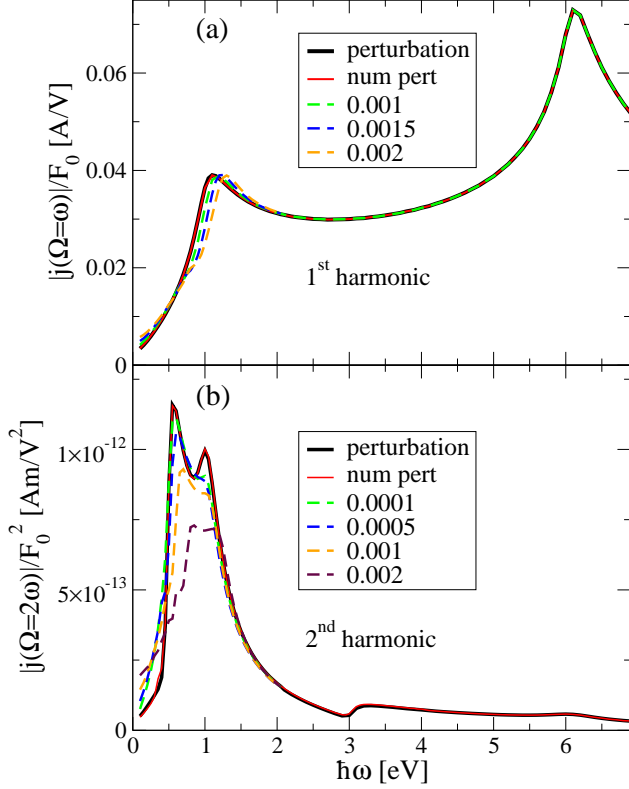


FIG. 3. The absolute value of the (a) first harmonic (linear response) and (b) second harmonic, for 1 eV gapped graphene and $\tau_1 = \tau_2 = 5$ fs, obtained using the condition (19) and compared to the perturbative result. The numbers in the legends in panels (a) and (b) denote the peak field strength (in a.u.) of the pulses used in the calculation. The curve labelled 'num pert' denotes the numerical result that compares best with the perturbation theory at peak fields (a) 10^{-4} a.u., and (b) 10^{-5} a.u., see the text.

dependence of n constant, equal to the initial value of n , i.e.,

$$n(\mathbf{k}, t) = n(\mathbf{k}, -\infty) = f_v(\mathbf{k}) - f_c(\mathbf{k}) = \Delta f_{vc}(\mathbf{k}). \quad (19)$$

Then, Eq. (11) is solved with the above condition to obtain the numerical result - this is essentially the solution in the Keldysh approximation [1]. Such an approximation is used for semiclassical analysis of high-order harmonic generation [6, 37] in order to simplify the theoretical analysis. The harmonic spectrum for the first and the second harmonic response is divided by F_0 and F_0^2 , respectively. The results of these calculations are given in Figs. 3 (a) and 3 (b), respectively.

The second set of numerical results, given in Fig. 4, is obtained when the equations of motions (11) and (12) are solved without application of the condition (19). In this way both the effects of depletion of the band occupation n and its coupling with the coherences ρ_{cv} are described.

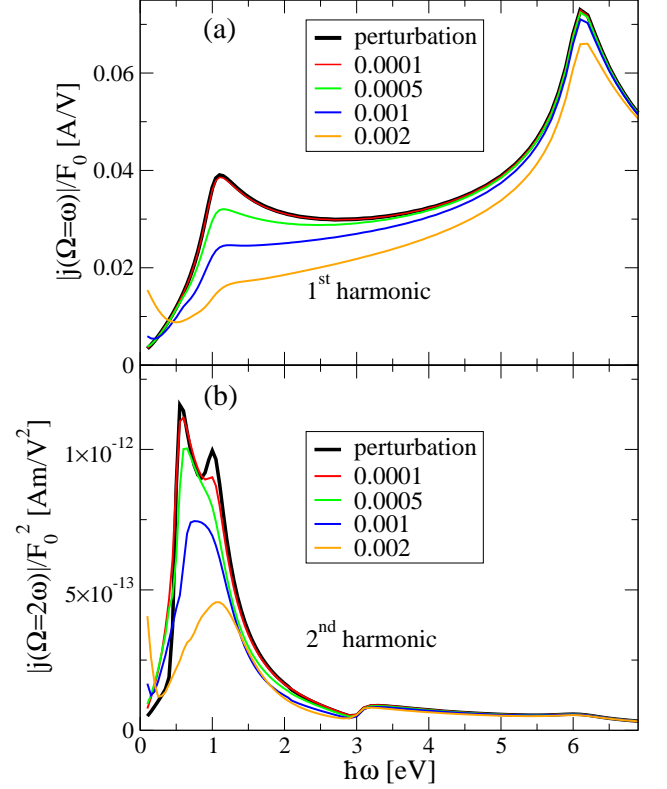


FIG. 4. The absolute value of the (a) first harmonic (linear response) and (b) second harmonic, for 1 eV gapped graphene and $\tau_1 = \tau_2 = 5$ fs, obtained with full calculation and compared to the perturbative result. The numbers in the legends in panels (a) and (b) denote the peak field strength (in a.u.) of the pulses used in the calculation.

We refer to this approach as the full calculation in the following.

We note that the perturbative first and the second harmonic responses [Eqs. (18)], derived from the equations of motion (11) and (12) with or without the approximation for constant n [Eq. (19)] are identical. Namely, the intra current from the second order in n is zero because an odd function of \mathbf{k} is integrated, since $p_{cc}(\mathbf{k}) = -p_{cc}(-\mathbf{k})$, $p_{vv}(\mathbf{k}) = -p_{vv}(-\mathbf{k})$, $|\xi_{cv}(\mathbf{k})|^2 = |\xi_{cv}(-\mathbf{k})|^2$, and $\Delta f_{vc}(\mathbf{k}) = \Delta f_{vc}(-\mathbf{k})$. Therefore the perturbative curve is used in both Figs. 3 and 4.

In Figs. 3 and 4 we compare the numerically obtained responses with the perturbative responses. To this end, we perform numerical calculations varying the peak field strength until a certain harmonic response as a function of frequency becomes 'frozen' for two consecutive field strengths. This, 'frozen' curve for both first and second harmonic response in Fig. 3 is denoted as 'num pert'. For the first harmonic this curve is obtained at a field strength of 10^{-4} a.u., whereas for the second harmonic that curve is obtained for a field strength one order of

magnitude smaller (10^{-5} a.u.). As evident from Fig. 3, the agreement of the numerically extracted harmonic responses with the perturbative responses is remarkable. Equally, in the case when we do not invoke the approximation for $n = \text{const.}$ [Fig. 4] we also obtain agreement with the perturbative result. We stress that the results from the full calculation are not fitted to the perturbative results, as done in Ref. [28].

V. TRANSITION TO THE NON-PERTURBATIVE REGIME

Gradually with the increase of the field strength, non-perturbative features appear in the numerical responses, starting at lower frequencies. This is visible in both cases: calculations using condition (19) [Fig. 3], and for the full calculation [Fig. 4]. In general, the peak field strengths at which there is deviation from the perturbative results are smaller for the second harmonic response than for the first harmonic response. Next, for the first harmonic response, when using the full calculation the deviation from the perturbative results (calculated at equal peak field strengths) is larger compared to the case when the condition of Eq. (19) is used; compare Figs. 3 (a) and 4 (a). In case of the second harmonic response this difference is not that large, however, it is non-negligible [Figs. 3 (b) and 4 (b)]. This is striking since in all our numerical calculations, during the time evolution, the depletion of n is at most 1% at the largest peak field strength used. This exposes the inadequacy of the approximation of Eq. (19) even at very small field strengths - in the discussion below we therefore use results obtained using the full calculation. Finally, while for the first harmonic the yield essentially decreases preserving the shape as the peak field strength increases, for the second harmonic response the modification is not only a decrease in magnitude but also the shape of the response is changed in such a way that the peaks at low energy (0.5 and 1 eV) merge into one rounded peak [Fig. 4 (b)]. We note that in the linear regime the ratio of the peak of the field generated by the n -th harmonic to the incident peak field F_0 is approximately equal to the ratio $|j(\Omega = n\omega)|/|j(\Omega = \omega)|$. For example for the second harmonic, in the worst case when $F_0 = 0.002$ a.u. is used, this ratio is of the order of 10^{-2} .

The departure from the perturbative regime can be illustrated for the third harmonic as well. In contrast to the first and the second harmonic, the perturbative limit for the third harmonic contains not only contribution from the inter part of the current, but also from the intra part of the current. Therefore the equations (18) are inadequate to describe the perturbative third harmonic generation and should be completed by adding equations for the coefficients $n^{(j)}$, $j \leq 3$, of the perturbative expansion of n , i.e.,

$$n(\mathbf{k}, t) = \sum_{j=1}^{\infty} F_0^j n^{(j)}(\mathbf{k}, t), \quad (20)$$

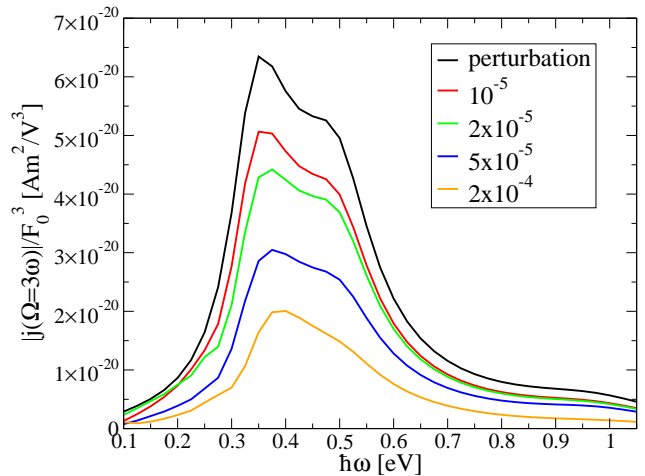


FIG. 5. The absolute value of the third harmonic for 1 eV gapped graphene, $\tau_1 = \tau_2 = 5$ fs, obtained at different peak field strengths and compared to the perturbative result. The numbers in the legend denote the peak field strength (in a.u.) of the $M = 48$ cycle pulses used in the calculation.

Then we insert the above expansion and the perturbative expansion of ρ in Eq. (17) in the equations of motion (11) and (12). This procedure results in adding the following equations for $n^{(2)}$ and $n^{(3)}$ ($n^{(0)} = \Delta f_{vc}(\mathbf{k})$ and $n^{(1)} = 0$)

$$\begin{aligned} \frac{dn^{(2)}}{dt} &= 2i \frac{e}{\hbar} \mathbf{f}(t) \cdot \left(\boldsymbol{\xi}_{cv} \rho_{cv}^{(1)*} - \boldsymbol{\xi}_{cv}^* \rho_{cv}^{(1)} \right) - \frac{n^{(2)}}{\tau_2} \\ \frac{dn^{(3)}}{dt} &= 2i \frac{e}{\hbar} \mathbf{f}(t) \cdot \left(\boldsymbol{\xi}_{cv} \rho_{cv}^{(2)*} - \boldsymbol{\xi}_{cv}^* \rho_{cv}^{(2)} \right) - \frac{n^{(3)}}{\tau_2} \\ &\quad + \frac{e}{\hbar} \mathbf{f}(t) \cdot (\nabla_{\mathbf{k}} n^{(2)}) \end{aligned} \quad (21)$$

to the system of equations (18) and modifying the equation for $\rho_{cv}^{(3)}$ as

$$\begin{aligned} \frac{d\rho_{cv}^{(3)}}{dt} &= -i\omega_{cv} \rho_{cv}^{(3)} - \frac{\rho_{cv}^{(3)}}{\tau_1} - i \frac{e}{\hbar} \mathbf{f}(t) \cdot (\boldsymbol{\xi}_{cc} - \boldsymbol{\xi}_{vv}) \rho_{cv}^{(2)} \\ &\quad + \frac{e}{\hbar} (\mathbf{f}(t) \cdot \nabla_{\mathbf{k}}) \rho_{cv}^{(2)} - i \frac{e}{\hbar} \mathbf{f}(t) \cdot \boldsymbol{\xi}_{cv} n^{(2)}. \end{aligned} \quad (22)$$

Using these equations, the perturbative third harmonic is obtained. In Fig. 5, this perturbative result (with $\tau_1 = \tau_2 = 5$ fs) is compared to the full numerical calculation at different peak field strengths for photon energies up to 1 eV, as for higher photon energies the response falls off rapidly to zero. The perturbative curve has peaks at photon energies corresponding to one third and one half of the gap. As the field increases, the height of the harmonic decreases and the peaks merge into one broad peak. The discrepancy between the full calculation and the perturbative result starts here at lower peak field strengths (at least as small as 10^{-6} a.u.) as compared to both the first and the second harmonic response.

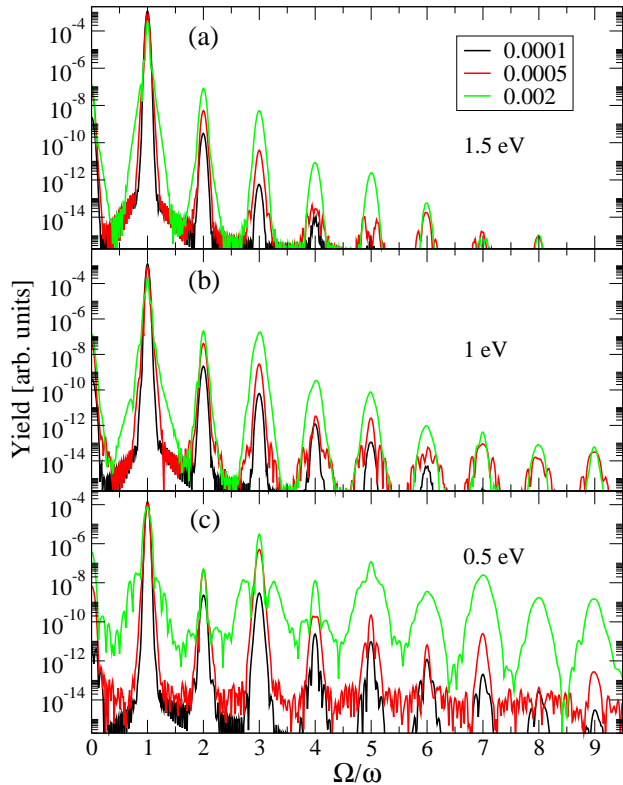


FIG. 6. Harmonic spectra (divided by peak field strength squared) for different peak fields (given in the legend in atomic units) at (a) $\hbar\omega = 1.5$ eV, (b) $\hbar\omega = 1$ eV, and (c) $\hbar\omega = 0.5$ eV photon energy. The yield is proportional to $|j(\Omega)|^2/F_0^2$.

Figure 6 shows what happens to the harmonic spectra after the field strength becomes large enough and/or the incident photon energy becomes small enough so that perturbation theory breaks down. We note that the harmonic spectra depicted in Fig. 6 are divided by the square of the peak field strength so that the first harmonic is at comparable height for different field strengths. In Fig. 6 (a) the situation for a photon energy of 1.5 eV is depicted. At the perturbative field strength of 10^{-4} a.u. the height of the higher harmonics rapidly falls off. This is also true for the next larger peak field strength in Fig. 6 (a). However, for the highest peak field strength, the fall-off is not so rapid and pairs of adjacent harmonics (2nd and 3rd, 4th and 5th) tend to almost level up in height. At a lower photon energy of 1 eV [Fig. 6 (b)] and at the largest peak field strength the beginning of a plateau, known to be typical for atoms and molecules [8, 38], is visible. For the lowest photon energy depicted [0.5 eV in Fig. 6 (c)], the harmonic spectrum forms a pronounced plateau for the two largest peak field strengths. The number of harmonics forming the plateau is roughly proportional to the peak field strength. This is in qual-

itative agreement with a semiclassical analysis for the harmonic cutoff [37], where it was predicted that it is proportional to F_0/ω . After the departure from the perturbative regime, due to the increase of this factor, the harmonic peaks start forming a plateau, which is a signature of non-perturbative dynamics.

The transition to the non-perturbative regime is also illustrated in Fig. 7, where harmonic spectra are given as two-dimensional plots of the harmonic order and the photon energy of the driving field in the interval from 0.1 to 2 eV, and for different field strengths. We present this figure to illustrate the growth of the harmonics at different photon energies as the peak field strength increases. A single horizontal line in Fig. 7 contains a harmonic spectrum of the type presented in Fig. 6. To qualitatively estimate the progression of harmonics as the peak field strength increases, the two-dimensional space (harmonic order, photon energy) is divided by three curves, corresponding to the borders of how many harmonics fit in (in order from left to right in Fig. 7) the 1eV gap, the gap corresponding to the van Hove singularity (6.2 eV), and the maximum gap (18.03 eV) in our two-band model.

The spectra for the smallest field strength [Fig. 7 (a)] contain well-pronounced harmonics which drop off in the (harmonic order, photon energy) region bounded by the curves corresponding to the gap and van Hove singularity, see the caption of Fig. 7. The harmonic peaks for the next larger peak strength [Fig. 7 (b)] drop off around the van Hove singularity curve. Lastly, the harmonics at the largest peak field strength considered [Fig. 7 (c)] drop off in the region bounded by the curves corresponding to the van Hove singularity and the maximum gap. The curve corresponding to the maximum gap is in fact the limit for harmonic generation in the present two-band model - no well-formed harmonic at any field strengths is situated to the right of this curve. We note that at the energy range occupied by the harmonics of higher orders the contribution from other bands may not be ignored. Here, however, we only consider the non-perturbative limit within the two band model.

Finally, we consider the gap dependence. For simplicity, we focus at photon energies corresponding to the gap ($\hbar\omega = \Delta$), where the major part of the first order response is located and where the deviation from the perturbative result is more pronounced. We aim to compare different gaps for field strengths that result in comparable values of the response. A possible scaling for the field strength emerges by considering that the leading order of the dependence of the dipole matrix element ξ_{cv} is Δ^{-1} . Assuming that this term is dominant in the differential equations of motion [Eqs. 11 and 12], when changing the gap Δ , a field $c\Delta F_0$, where c is a constant, will give roughly, but not exactly, the same response. To limit the total duration of the numerical time propagation, we consider pulses with $M = 12$ which are long enough to be free from few-cycle effects. Similarly to Ref. [16], we use an asymmetric decoherence times, with $\tau_1 = 10$ fs

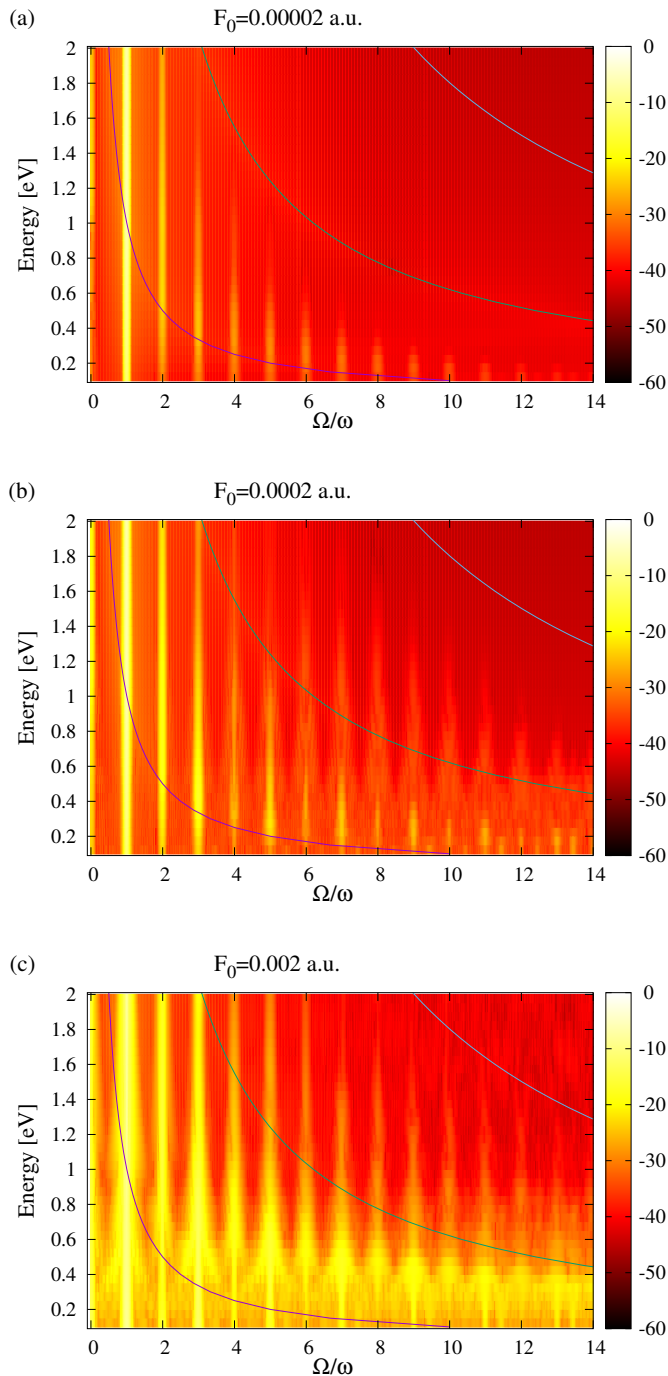


FIG. 7. Harmonic spectra (divided by peak field strength squared) at different photon energies of the driving field on color logarithmic scale in arbitrary units. (a) spectra for a peak field strength of 2×10^{-5} a.u. (close to the perturbation regime), (b) spectra for a peak field strength of 2×10^{-4} a.u., and (c) spectra for a peak field strength of 2×10^{-3} a.u. (deeply in the non-perturbative regime). The lines in the color plots denote the borders defining how many harmonics fit (in order from left to right on the figure) at the 1 eV gap (K point), at the 6.2 eV gap at van Hove singularity (M point), and at the maximum gap of 18.03 eV (Γ point).

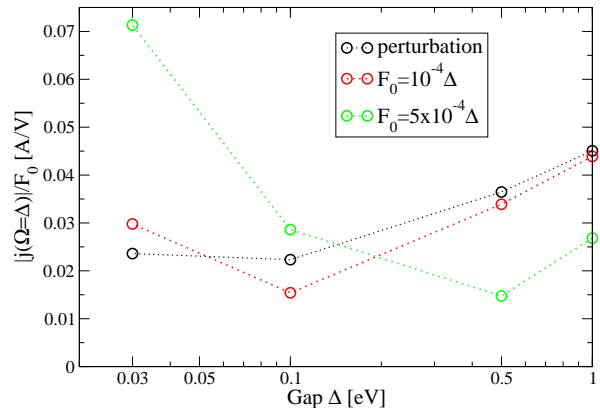


FIG. 8. First harmonic at the photon energy equal to the gap ($\hbar\omega = \Delta$). The peak field strengths (scaled to the gap) are given in a.u. in the legend. To obtain the actual field strength in a.u. used for a given gap, Δ in the legend should be given in eV.

and $\tau_2 = 1$ ps. The results of the calculations are shown in Fig. 8. The scaled first harmonics in the figure are of the same order of magnitude, which justifies the scaling of the field strength. Moreover, as the gap decreases the perturbative result (obtained using Eqs. (18)) becomes more flat, reflecting the fact that the term ξ_{cv} becomes more dominant in the equations of motion. From the other curves, the rough scaling of the peak field strength at which the perturbation theory breaks down can be deduced. Namely, the curve corresponding to the peak field strength that gives almost perturbative result at 1eV gap (the curve labelled with $F_0 = 10^{-4} \Delta$ in Fig. 8) becomes a bit more non-perturbative as the gap decreases. Hence, for the first harmonic, it is safe to assume that if there is a deviation between the perturbative result and the full calculation at 1 eV, this deviation will be even larger for the gaps at an equivalent scaled peak electric field. For a larger field strength (the curve labelled with $F_0 = 5 \times 10^{-4} \Delta$ in Fig. 8), the result is already deep in the non-perturbative regime for a gap of 1eV, and at smaller gaps it enters even deeper in the non-perturbative regime.

In closing, we consider the gap dependence of the second harmonic in Fig. 9. This is interesting since in the limit of zero gap the second-order harmonic vanishes. To investigate this limit it is easier to use the frequency-domain method than the time-dependent one since as the gap decreases larger grids in \mathbf{k} -space should be taken and the pulses should be propagated for longer times, which becomes prohibitively time-consuming. Therefore in Fig. 9, where we plot the second harmonic at a driving photon frequency equal to the gap and to the half of the gap, respectively, we used the frequency-domain

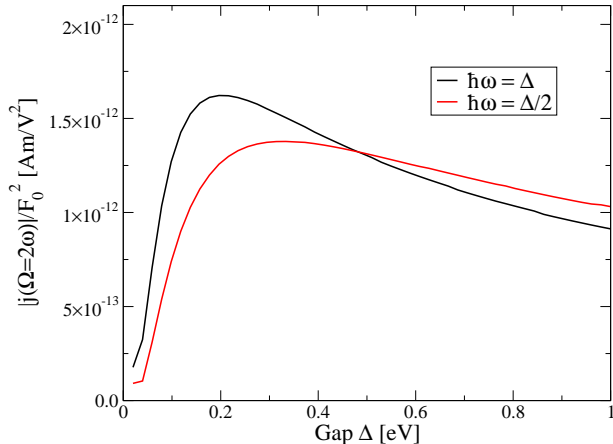


FIG. 9. Second harmonic at the photon energy equal to the gap ($\hbar\omega = \Delta$) and at photon energy equal to the half of the gap ($\hbar\omega = \Delta/2$), obtained using the frequency-domain method of Ref. [26], $\tau_1 = \tau_2 = 5$ fs, and 6000×6000 grid in \mathbf{k} -space.

method of Ref. [26]. We applied the same scaling factors as for the results from the frequency-domain method presented in Fig. 2 (b). As the gap decreases, the height of the second harmonic first increases, reaching a peak at approximately at 0.2 eV for the case of $\hbar\omega = \Delta$ and approximately at 0.3 eV for the case of $\hbar\omega = \Delta/2$, and then falls towards zero. This is so since as the gap starts decreasing, (i) the energies in the denominators of the expression for the second order conductivity [Eq. (27) in Ref. [26]] become small, but also (ii) the numerators of the same expression become smaller as the centrosymmetric limit is approached. Eventually, the numerator wins and the second harmonic current goes to zero. The same was observed for the second harmonic in carbon nanotubes [39] as the radius of the tube increases and the tube approaches the planar graphene limit.

VI. CONCLUSIONS AND OUTLOOK

We have explored the limit of perturbative harmonic response, which is usually considered for infinitely periodic pulses, in the time domain, and demonstrated excellent agreement between the numerical calculation and perturbation theory for low laser intensity over the interval of photon energies that includes all features in the spectrum. The numerical method for perturbative harmonic responses is especially well-suited to obtain not only the first few harmonics, but also high-order harmonics for realistic, finite-duration pulses.

Comparing with the full non-perturbative calculations, we conclude that the harmonic response starts to deviate from the perturbative harmonic response at relatively

low field strengths. The calculation performed for constant difference in the occupation of the valence and the conduction band fails to reproduce the correct point of departure from the perturbative result even for the first harmonic, which exposes its weakness.

Finally, we have illustrated the transition from the perturbative to the non-perturbative regime in the harmonic spectra. For each harmonic, the breakdown of perturbation theory occurs at different field strength, which is smaller for the second harmonic than for the first harmonic. For the third harmonic the perturbation theory breaks down at even smaller field strengths. Increasing the field strength further, the harmonics start forming the typical HHG plateau, well-studied in the strong-field physics for atoms and molecules. In contrast to atoms and molecules, the plateau cut-off is here limited by the maximum gap since the analysis was performed in a two-band approximation. At the end, we have considered the gap dependence for the linear response using simple scaling, and illustrated the transition to the non-perturbative regime.

As strong-field physics with its intense near-infrared laser pulses of femtosecond duration is extended from atoms and molecules to condensed matter systems [5], and with the advent of high-harmonic spectroscopy for solids [40], the development of theory that is explicitly time-dependent and capable of dealing with the laser-matter interaction in a non-perturbative manner is essential. Here we provided a candidate for such a theory which, in this work, was validated by comparison with the results of perturbation theory. The formulation can be extended to multiple bands, combination of pulses, other materials, and to include the Coulomb interaction. It is probably in these contexts that the coherence properties of the laser light and the ability to perform pump-probe experiments and simulations will show its full potential for gaining time-resolved insight in ultrafast dynamics in solids.

ACKNOWLEDGEMENTS

This work was supported by the Villum Kann Rasmussen (VKR) center of excellence, QUSCOPE. The numerical results were obtained at the Centre for Scientific Computing, Aarhus.

APPENDIX: DIPOLE AND MOMENTUM MATRIX ELEMENTS

A. Dipole matrix elements (ξ_{nm})

The eigenvectors of the Hamiltonian $\hat{\mathbf{H}}_0$ of Eq. (2) are

$$|n\rangle = \frac{1}{\sqrt{2}} \begin{pmatrix} \sqrt{(E_n + \Delta/2)/E_n} \\ \pm e^{-i\phi(\mathbf{k})} \sqrt{(E_n - \Delta/2)/E_n} \end{pmatrix}, \quad (23)$$

where $|n\rangle$ denotes either the states in the conduction ($|c\rangle$) or the valence band ($|v\rangle$), E_n denotes either E_c or E_v , ' \pm ' is '+' for the conduction and '-' for the valence band, respectively, and

$$\phi(\mathbf{k}) = \text{Arg}[f(\mathbf{k})], \quad (24)$$

with $f(\mathbf{k})$ given in Eq. (3).

The dipole matrix elements ξ_{cv} and $\xi_{cc} - \xi_{vv}$, used in the main text, are obtained by direct calculation, i.e., by calculating $\langle n | i\nabla_{\mathbf{k}} | m \rangle$, $n, m = c, v$. They are explicitly given by

$$\text{Re}\{\xi_{cv}\} = \frac{a\gamma}{2E_c|f(\mathbf{k})|} \left[\frac{1}{\sqrt{3}} \left(\cos(ak_x\sqrt{3}/2) \cos(ak_y/2) - \cos(ak_y) \right) \mathbf{e}_x + \sin(ak_x\sqrt{3}/2) \sin(ak_y/2) \mathbf{e}_y \right], \quad (25)$$

$$\text{Im}\{\xi_{cv}\} = \frac{a\Delta\gamma}{4E_c^2|f(\mathbf{k})|} \left[\sqrt{3} \sin(ak_x\sqrt{3}/2) \cos(ak_y/2) \mathbf{e}_x + \left(\cos(ak_x\sqrt{3}/2) \sin(ak_y/2) + \sin(ak_y) \right) \mathbf{e}_y \right], \quad (26)$$

and

$$\xi_{cc} - \xi_{vv} = -\frac{a\Delta}{2\sqrt{3}E_c|f(\mathbf{k})|^2} \left[\left(\cos(ak_x\sqrt{3}/2) \cos(ak_y/2) - \cos(ak_y) \right) \mathbf{e}_x + \sin(ak_x\sqrt{3}/2) \sin(ak_y/2) \mathbf{e}_y \right]. \quad (27)$$

B. Momentum matrix elements (\mathbf{p}_{nm})

The diagonal momentum matrix elements are obtained as $\mathbf{p}_{nn} = \frac{m_e}{\hbar} \frac{\partial E_n}{\partial \mathbf{k}}$ yielding

$$\mathbf{p}_{cc} = -\frac{m_e}{\hbar} \frac{a\gamma^2}{E_c} \left[\sqrt{3} \sin(ak_x\sqrt{3}/2) \cos(ak_y/2) \mathbf{e}_x + \left(\cos(ak_x\sqrt{3}/2) \sin(ak_y/2) + \sin(ak_y) \right) \mathbf{e}_y \right], \quad \mathbf{p}_{vv} = -\mathbf{p}_{cc}. \quad (28)$$

The off-diagonal matrix element \mathbf{p}_{cv} is simply obtained using

$$\mathbf{p}_{cv} = i \frac{m_e}{\hbar} (E_c - E_v) \xi_{cv}. \quad (29)$$

-
- [1] L. V. Keldysh, Sov. Phys. JETP **20**, 1307 (1965)
 - [2] F. Krausz and M. I. Stockman, Nat Photon **8**, 205 (2014)
 - [3] A. Schiffrin, T. Paasch-Colberg, N. Karpowicz, V. Apalkov, D. Gerster, S. Muhlbrandt, M. Korbman, J. Reichert, M. Schultze, S. Holzner, J. V. Barth, R. Kienberger, R. Ernstorfer, V. S. Yakovlev, M. I. Stockman, and F. Krausz, Nature **493**, 70 (2013)
 - [4] H. K. Kellardeh, V. Apalkov, and M. I. Stockman, Phys. Rev. B **91**, 045439 (2015)
 - [5] S. Ghimire, A. D. DiChiara, E. Sistrunk, P. Agostini, and D. A. DiMauro, Louis F. Reis, Nat Phys **7**, 138 (2011)
 - [6] G. Vampa, C. R. McDonald, G. Orlando, D. D. Klug, P. B. Corkum, and T. Brabec, Phys. Rev. Lett. **113**, 073901 (2014)
 - [7] A. K. Geim and K. S. Novoselov, Nat Mater **6**, 183 (2007)
 - [8] M. Lewenstein, P. Balcou, M. Y. Ivanov, A. L'Huillier, and P. B. Corkum, Phys. Rev. A **49**, 2117 (1994)
 - [9] S. I. Simonsen, S. A. Sørngård, M. Førre, and J. P. Hansen, Journal of Physics B: Atomic, Molecular and Optical Physics **47**, 065401 (2014)
 - [10] J. Guo, H. Zhong, B. Yan, Y. Chen, Y. Jiang, T.-f. Wang, J.-f. Shao, C.-b. Zheng, and X.-S. Liu, Phys. Rev. A **93**, 033806 (2016)
 - [11] I. Al-Naib, J. E. Sipe, and M. M. Dignam, Phys. Rev. B **90**, 245423 (2014)
 - [12] K. L. Ishikawa, Phys. Rev. B **82**, 201402 (2010)
 - [13] H. K. Avetissian, A. K. Avetissian, G. F. Mkrtchian, and K. V. Sedrakian, Phys. Rev. B **85**, 115443 (2012)
 - [14] H. K. Avetissian, A. K. Avetissian, G. F. Mkrtchian, and K. V. Sedrakian, Journal of Nanophotonics **6**, 061702 (2012)
 - [15] H. K. Avetissian, G. F. Mkrtchian, K. G. Batrakov, S. A. Maksimenko, and A. Hoffmann, Phys. Rev. B **88**, 165411 (2013)
 - [16] J. L. Cheng, N. Vermeulen, and J. E. Sipe, Phys. Rev.

- B **91**, 235320 (2015)
- [17] H. Rostami and M. Polini, Phys. Rev. B **93**, 161411 (2016)
- [18] S. Y. Zhou, G.-H. Gweon, A. V. Fedorov, P. N. First, W. A. de Heer, D.-H. Lee, F. Guinea, A. H. Castro Neto, and A. Lanzara, Nat Mater **6**, 770 (2007)
- [19] E. V. Castro, K. S. Novoselov, S. V. Morozov, N. M. R. Peres, J. M. B. L. dos Santos, J. Nilsson, F. Guinea, A. K. Geim, and A. H. C. Neto, Phys. Rev. Lett. **99**, 216802 (2007)
- [20] X. Li, X. Wang, L. Zhang, S. Lee, and H. Dai, Science **319**, 1229 (2008)
- [21] T. G. Pedersen, C. Flindt, J. Pedersen, N. A. Mortensen, A.-P. Jauho, and K. Pedersen, Phys. Rev. Lett. **100**, 136804 (2008)
- [22] T. G. Pedersen, C. Flindt, J. Pedersen, A.-P. Jauho, N. A. Mortensen, and K. Pedersen, Phys. Rev. B **77**, 245431 (2008)
- [23] T. G. Pedersen, A.-P. Jauho, and K. Pedersen, Phys. Rev. B **79**, 113406 (2009)
- [24] P. K. Pyatkovskiy, Journal of Physics: Condensed Matter **21**, 025506 (2009)
- [25] A. Singh, T. Satpati, K. I. Bolotin, S. Ghosh, and A. Agarwal, ArXiv e-prints (2016), arXiv:1606.05072 [cond-mat.mes-hall]
- [26] T. G. Pedersen, Phys. Rev. B **92**, 235432 (2015)
- [27] S. A. Jafari, Journal of Physics: Condensed Matter **24**, 205802 (2012)
- [28] J. L. Cheng, N. Vermeulen, and J. E. Sipe, Phys. Rev. B **92**, 235307 (2015)
- [29] J. G. Pedersen and T. G. Pedersen, Phys. Rev. B **84**, 115424 (2011)
- [30] P. R. Wallace, Phys. Rev. **71**, 622 (1947)
- [31] V. A. Margulis, E. E. Muryumin, and E. A. Gaiduk, Phys. Rev. B **77**, 035425 (2008)
- [32] C. Aversa and J. E. Sipe, Phys. Rev. B **52**, 14636 (1995)
- [33] T. G. Pedersen, Phys. Rev. B **67**, 113106 (2003)
- [34] T. G. Pedersen, K. Pedersen, and T. Brun Kristensen, Phys. Rev. B **63**, 201101 (2001)
- [35] R. W. Boyd, ed., *Nonlinear Optics (Third Edition)* (Academic Press, Burlington, 2008)
- [36] L. Van Hove, Phys. Rev. **89**, 1189 (1953)
- [37] G. Vampa, C. R. McDonald, G. Orlando, P. B. Corkum, and T. Brabec, Phys. Rev. B **91**, 064302 (2015)
- [38] P. B. Corkum, Phys. Rev. Lett. **71**, 1994 (1993)
- [39] T. G. Pedersen, and K. Pedersen, Phys. Rev. B **79**, 035422 (2009)
- [40] T. T. Luu, M. Garg, S. Y. Kruchinin, A. Moulet, M. T. Hassan, and E. Goulielmakis, Nature **521**, 498 (2015)